Supporting Information

Single-Molecule-Like Intramolecular Charge Transfer in Multi-Nitrogen Hybridization HOF for Selective Water Detection

Yixin Chen[†a], Zhuoyan Dong[†a], Qianni Peng[a], Gaoyan Lan[a], Difeng Yang[a], Zizhu Yao[ac], Kang Wang[b], Shengchang Xiang[a], Yuanchao Lv*[a] and Zhangjing Zhang*[a]

[a]Fujian Key Laboratory of Polymer Materials, College of Chemistry and Materials Science, Fujian Normal University, Fuzhou 350007, China

[b]Key Laboratory of Photochemistry, Institute of Chemistry, Chinese Academy of Sciences, Beijing 100190, China; School of Chemical Sciences, University of Chinese Academy of Sciences, Beijing 100049, China

[c]State Key Laboratory of Structural Chemistry, Fujian Institute of Research on the Structure of Matter, Chinese Academy of Sciences, Fuzhou, Fujian 350002, PR China

*E-mail: lvyc@fjnu.edu.cn; zzhang@fjnu.edu.cn

Contents

xxviii. **Figure S25.** Schematic diagram of the homemade setup used to measure the humidity sensor performance at 98% RH.

xxix. **Figure S26.** Real-time dynamic response-recovery curves of **HOF-FJU-167** when alternating dry N_2 and 98 % RH N_2.

xxx. **Table S1.** Crystal data and structure refinement for the **HOF-FJU-167** (CCDC No. 2502738), **HOF-FJU-167H** (CCDC No. 2502741), **HOF-FJU-167ACE** (CCDC No. 2502742), and **HOF-FJU-169** (CCDC No. 2502743).

xxxi. **Table S2.** Emission maxima of **HOF-FJU-167** under the stimulation of different solvent atmospheres.

xxxii. **Table S3.** Emission maxima of **HOF-FJU-167** under different humidity conditions.

Experimental details

1. Materials

The 5,5',5''-(nitrilotris(benzene-4,1-diyl))tripicolinonitrile (5-NBDTP) and 4,4',4''-(nitrilotris(benzene-4,1-diyl))tripicolinonitrile (4-NBDTP) were synthesized through the classical Suzuki condensation reaction. Tris(4-Bromophenyl) Amine, 2-Cyanopyridine-5-Boronic Acid Pinacol Ester,3-Cyanopyridine-5-boronic acid pinacol ester, $PdCl_2$ (Dppf), and K_2CO_3 were purchased from Aldrich Chemical Co., and used without further purification. Organic solvents, Toluene (TOL), Acetonitrile (ACN), Dichloromethane (DCM), Isopropanol (IPA), (Acetone) ACE, Ethyl acetate (EA), Ethanol (EtOH), Methanol (MeOH), Dimethyl sulfoxide (DMSO), N, N-Dimethylformamide (DMF), and Petroleum ether (PE), were dried and distilled before use.

2. Synthesis of the **HOF-FJU-167** and **HOF-FJU-167ACE** crystals.

The **HOF-FJU-167** was prepared by a liquid-phase self-assembly experiment in EA. As for **HOF-FJU-167**, the 5-NBDTP (0.005 g, 0.0075 mmol) was dissolved in EA (1 mL) in a 5 mL brown glass vial under heating at 90 °C to get a clear solution. Then the solution was allowed to cool to room temperature slowly, and lozenge single crystals of **HOF-FJU-167** were obtained. The **HOF-FJU-167ACE** was prepared by a liquid-phase self-assembly experiment in ACE. As for **HOF-FJU-167ACE**, the 5-NBDTP (0.005 g, 0.0075 mmol) was dissolved in ACE (0.5 mL) in a 5 mL brown glass. Then the solution was allowed to evaporate at room temperature, and lozenge single crystals of **HOF-FJU-167** were obtained. Besides, the thickness and size of the **HOF-FJU-167** and **HOF-FJU-167ACE** are determined by the precipitation time and the concentration of the solution, and the ideal size and thickness of the crystal can be obtained by adjusting the cooling time and concentration. Thus, we could finely tune the thickness and size by changing the concentration of 5-NBDTP in EA from 3 to 5 mg mL^{-1} and utilizing the gradient cooling.

3. Synthesis of the **HOF-FJU-169** crystal.

The **HOF-FJU-169** was prepared by a liquid-phase self-assembly experiment in DCM. As for **HOF-FJU-169**, the 4-NBDTP (0.005 g, 0.0075 mmol) was dissolved in DCM (1 mL) in a 5 mL brown glass vial to obtain a clear solution. Then the solvent was allowed to evaporate slowly at room temperature, and the green rod-shaped single crystals of **HOF-FJU-169** were obtained.

4. Calculation methods

The electronic structures of the ground and excited states were calculated at the level of B3LYP/6-31g(d) using the Gaussian 09 software package. The molecular electrostatic potential was calculated in Multiwfn. The framework dipole moment and sorption were simulated in Materials Studio.

5. Characterizations

^{1}H-NMR spectra were recorded on a Bruker Advance III 600 MHZ spectrometer. Powder X-ray diffraction (PXRD) patterns were performed on a PANalytical X'Pert^{3} powder diffractometer at 40 kV, 40 mA for Cu Kα (λ= 1.54056 Å) with a scan range from 5 to 30 °. The simulated PXRD pattern was produced using the Mercury V2.2 program from single-crystal diffraction data. In-situ diffuse reflectance infrared spectra were recorded in the 800-4000 cm^{-1} range on a VERTEX 70v spectrophotometer. UV–Visible absorption spectra were measured using a Shimadzu UV2600 spectrophotometer. Fluorescence spectra were measured on a fluorescence spectrophotometer (FS5, Edinburgh Instruments Ltd., UK). Bright-field optical images and fluorescence microscopy images were taken from an inverted fluorescence microscope (Nikon Ti2), by exciting the samples with a mercury lamp. The guest-free sample was analyzed using a Micromeritics ASAP 2020 HD88 surface area analyzer to measure the gas adsorption isotherms. The PL signals from the **HOF-FJU-167**, **HOF-FJU-167H**, and **HOF-FJU-167ACE** were long-pass filtered at 400 nm to remove the excitation light, then dispersed with a grating and recorded with a spectrometer (PG2000-Pro, Ideaoptics Instruments). Thermogravimetric analysis (TGA) was performed on a METTLER Q50 analyzer under nitrogen or oxygen atmosphere with a heating rate of 10 ℃ min^{-1} from 30 ℃ to 600 ℃.

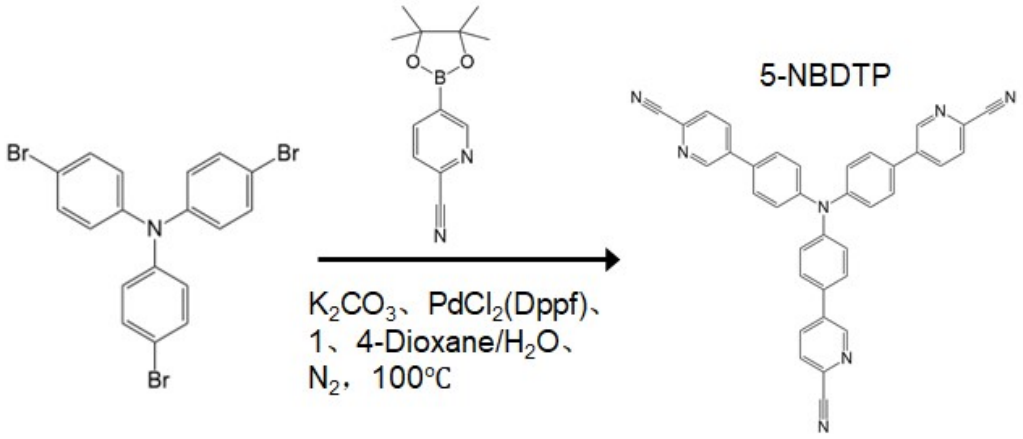

Scheme S1. Synthetic route of the 5-NBDTP molecule.

Tris(4-Bromophenyl) Amine (1 g, 2.074 mmol) and 2-Cyanopyridine-5-Boronic Acid Pinacol Ester (1.575 g, 6.84 mmol), $PdCl_2$ (dppf) (100 mg, 0.55 mmol), K_2CO_3 (1.5 g, 15 mmol) were added into a flask under nitrogen. Then 30 mL 1,4-dioxane and 6 mL pure water were injected by a syringe and refluxed at 100 ℃ for 24 h. After cooling to room temperature, the product was evaporated under high vacuum and then extracted with dichloromethane (3 × 100 mL). The organic phase was washed with water, dried with anhydrous sodium sulfate, and concentrated. The final powder product was purified by column chromatography, with DCM/PE as the mobile phase to give 5-NBDTP as a yellow solid (960 mg, 89.5 %). ^{1}H NMR (600 MHz, DMSO) δ 9.12 (d, J = 2.3 Hz, 1H), 8.35 (dd, J = 8.1, 2.3 Hz, 1H), 8.12 (d, J = 8.1 Hz, 1H), 7.88 (d, J = 8.4 Hz, 2H), 7.26 (d, J = 8.4 Hz, 2H).

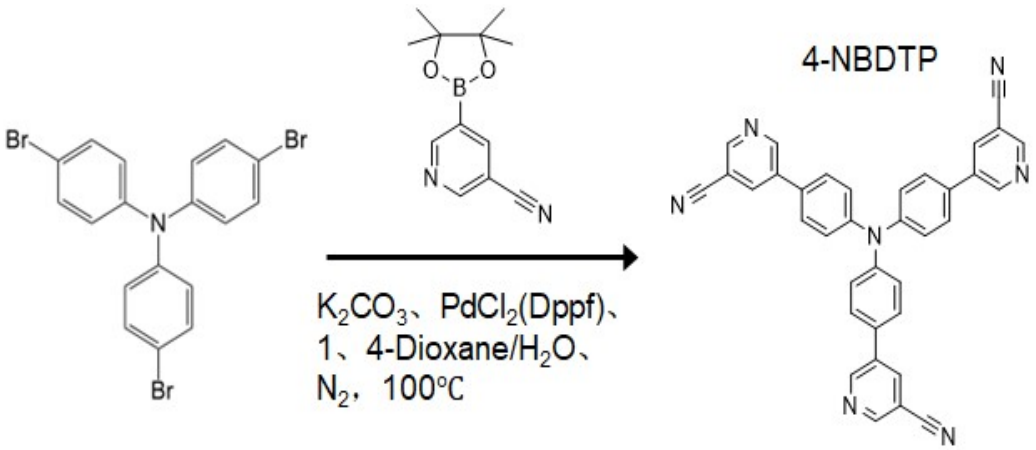

Scheme S2. Synthetic route of the 4-NBDTP molecule.

Tris(4-Bromophenyl) Amine (1 g, 2.074 mmol) and 3-Cyanopyridine-5-Boronic Acid Pinacol Ester (1.575 g, 6.84 mmol), $PdCl_2$ (dppf) (100 mg, 0.55 mmol), K_2CO_3 (1.5 g, 15 mmol) were added into a flask under nitrogen. Then 30 mL 1,4-dioxane and 6 mL pure water were injected by a syringe and refluxed at 100 ℃ for 24 h. After cooling to room temperature, the product was evaporated under high vacuum and then extracted with dichloromethane (3 × 100 mL). The organic phase was washed with water, dried with anhydrous sodium sulfate, and concentrated. The final powder product was purified by column chromatography, with DCM/PE as mobile phase to give 4-NBDTP as a yellow solid (752 mg, 73.2 %).^{1}H NMR (600 MHz, DMSO) δ 8.74 (d, J = 5.2 Hz, 1H), 8.39 (d, J = 1.9 Hz, 1H), 8.04 (dd, J = 5.3, 1.9 Hz, 1H), 7.96-7.90 (m, 2H), 7.26-7.18 (m, 2H).

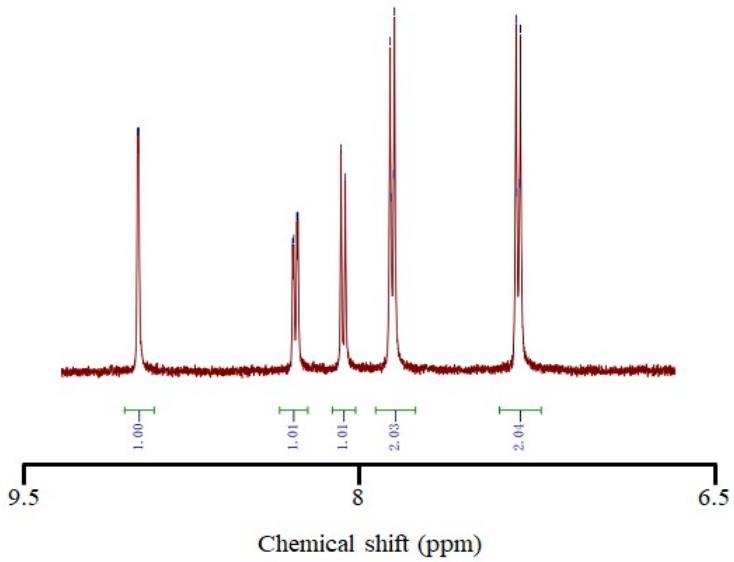

Figure S1. 1H-NMR spectra of the 5-NBDTP in DMSO-d6.

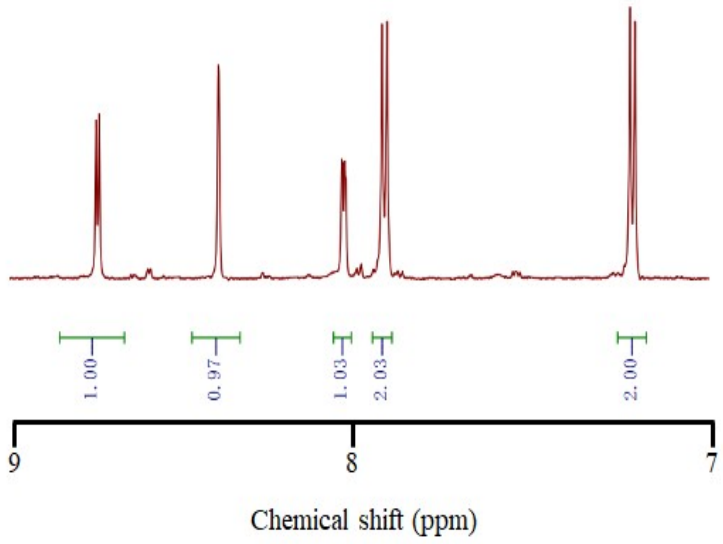

Figure S2. 1H-NMR spectra of the 4-NBDTP in DMSO-d6.

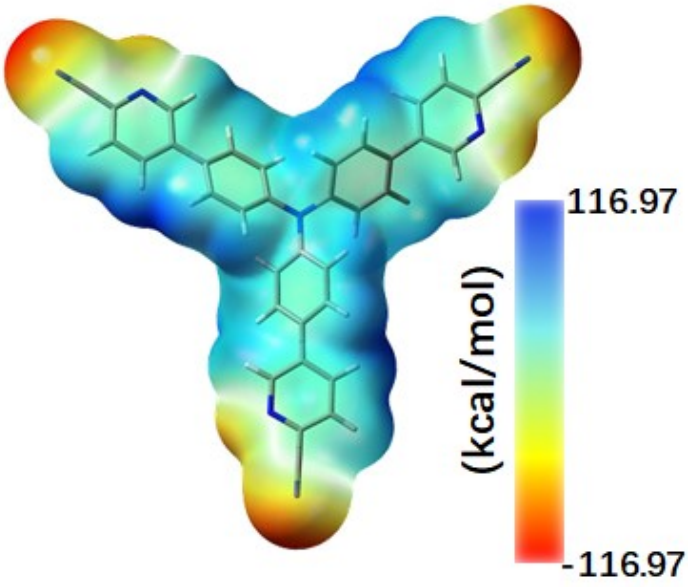

Figure S3. Electrostatic potential simulation of the 5-NBDTP.

The results of the electrostatic potential simulation indicate that both pyridine groups and cyano groups exhibit strong electronegative characteristics, which confirms that the hybrid nitrogen-doped functional moieties possess high reactivity.

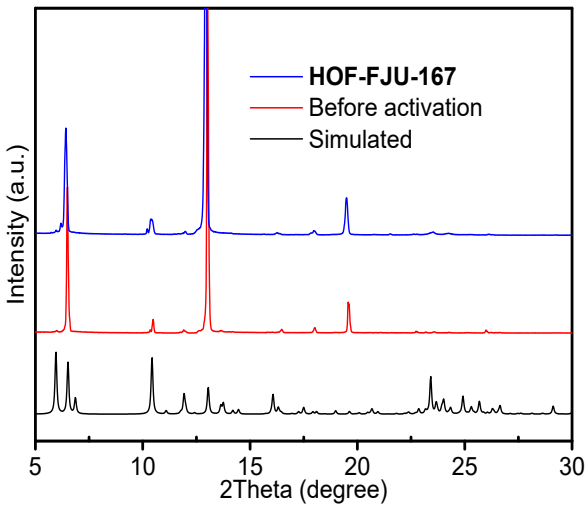

Figure S4. PXRD pattern of **HOF-FJU-167 (**simulated), **HOF-FJU-167** (before activation), and **HOF-FJU-167**.

Powder X-ray diffraction (PXRD) patterns indicate that as-synthesized **HOF-FJU-167** exhibits a pure-phase characteristic, and its pore size is found to increase slightly after activation.

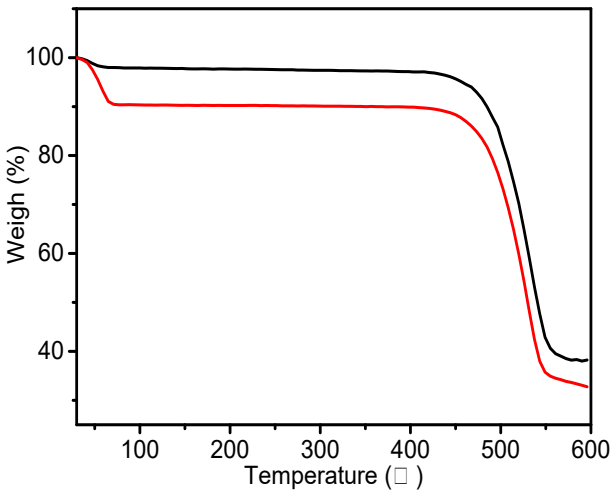

Figure S5. TGA curves of **HOF-FJU-167** and **HOF-FJU-167** (before activation) under N_2 atmosphere.

Thermogravimetric analysis (TGA) results confirm the successful activation of **HOF-FJU-167**, with the minor weight loss observed at the initial stage of the curve ascribed to the removal of adsorbed water molecules.

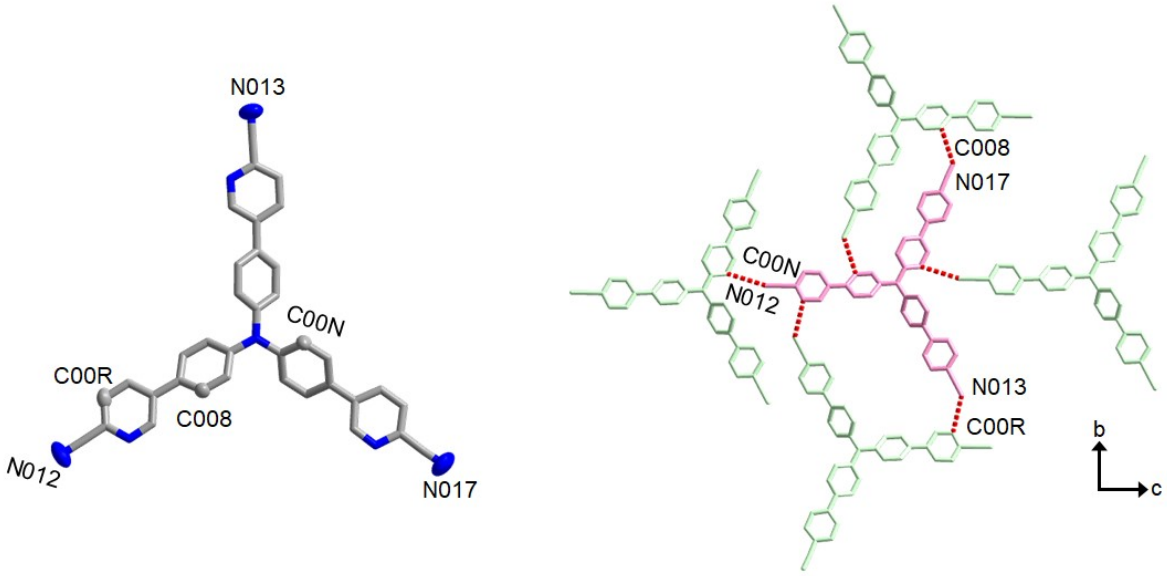

Figure S6. Schematic illustration of the molecule of the 5-NBDTP, the intermolecular hydrogen bonds of **HOF-FJU-167** (2D layer).

An asymmetric unit is connected to the surrounding four molecules through three pairs of hydrogen bonds to form a two-dimensional layer, namely C00N-N012, C00R-N013, and C008-N017.

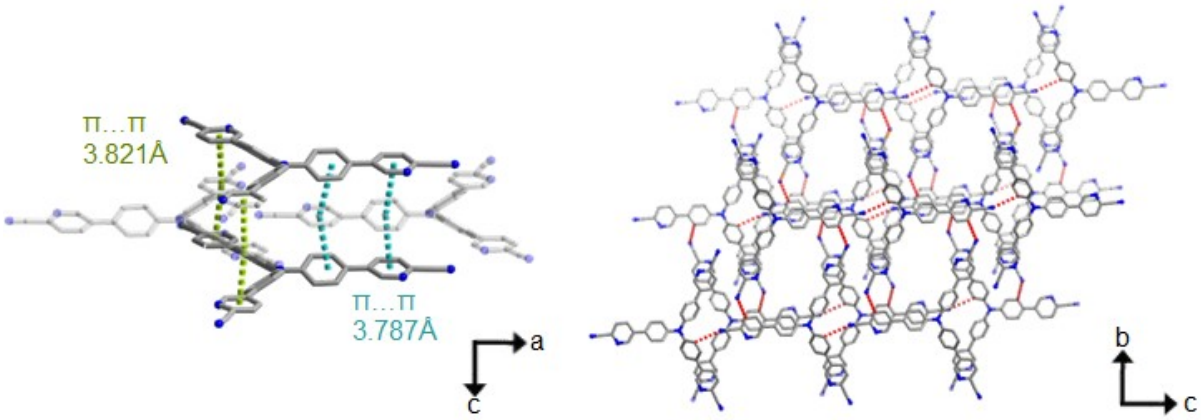

Figure S7. The interlayer π-π interactions and the three-dimensional (3D) framework structure of **HOF-FJU-167.**

The left one shows the two pairs of π-π forces between the layers, which offer a fixed connection between the two layers. And the right shows the entire three-dimensional framework, which is stacked through the type of A…B…A and displays a unique three-dimensional porous structure.

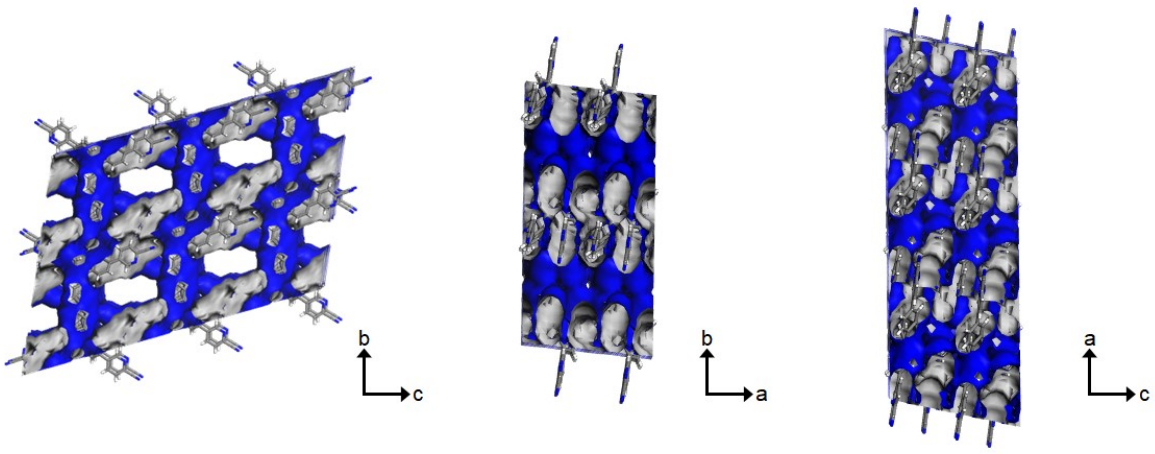

Figure S8. Schematic diagram of the **HOF-FJU-167** along different axial channels.

The orderly three-dimensional skeleton is formed by intermolecular hydrogen bonds of the building units and the interlayer π-π stacking. **HOF-FJU-167** has 1D open channels with a pore aperture size of 4 × 7 Å².

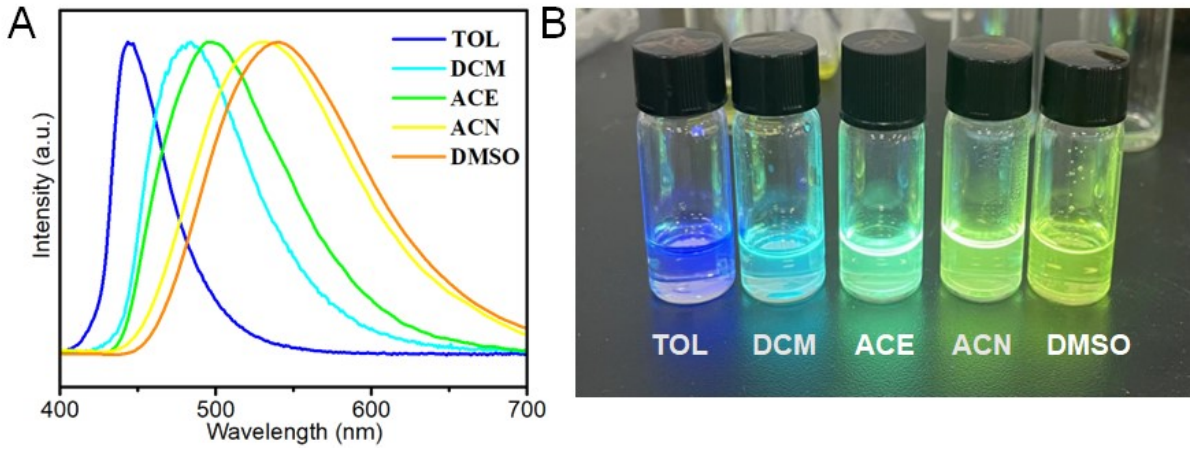

Figure S9. The PL spectra (A) and PL image (B) of dissolving the 5-NBDTP ligand in different polarity solvents.

The fluorescence spectral shift confirms a pronounced polarity-sensitive effect of the 5-NBDTP molecules. When the solvent polarity gradually increased from TOL to DMSO, the emission peaks of 5-NBDTP solutions showed considerable red shifts, which indicates that 5-NBDTP exhibits obvious intramolecular charge transfer characteristics. The discovery of this liquid-phase intramolecular charge transfer (ICT) process provides a foundation for investigating the effects of framework ICT.

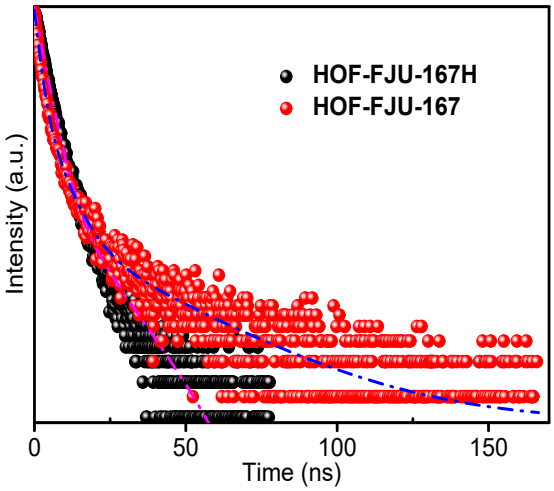

Figure S10. PL decay profiles of **HOF-FJU-167** and **HOF-FJU-167H**.

The photoluminescence (PL) decay profiles compared the fluorescence lifetime of **HOF-FJU-167** and **HOF-FJU-167H**, which shows a lifetime attenuation of **HOF-FJU-167H**, indicating that the intramolecular charge transfer process (ICT) was enhanced after the interaction between the framework and water.

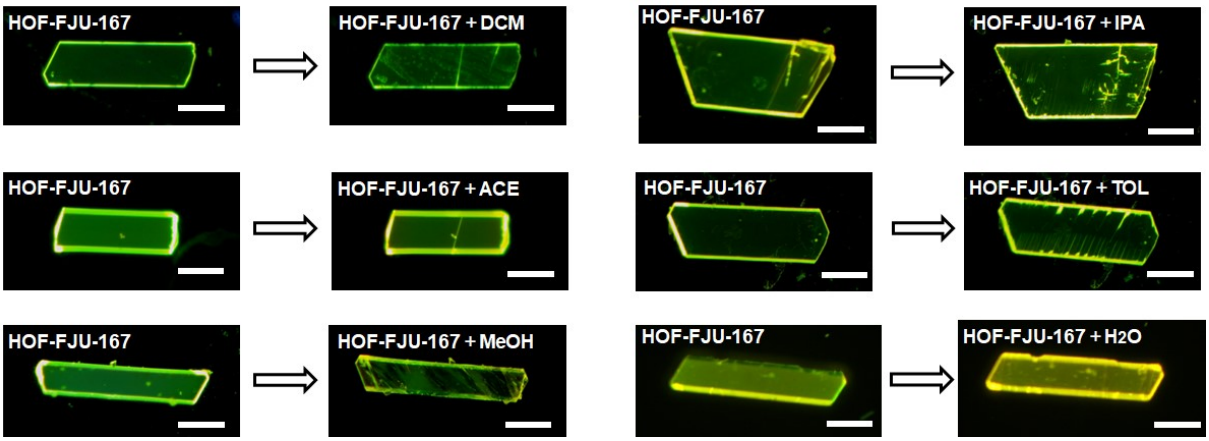

Figure S11. The PL images of **HOF-FJU-167** before/after stimulation with different polarity solvents. Scale bar: 50 μm.

The photoluminescence (PL) images of **HOF-FJU-167** before/after stimulation with different solvents intuitively demonstrate that this material undergoes a specific redshift change upon water stimulation. This is attributed to the steric hindrance effect of the framework, which enables the framework to achieve a saturated intramolecular charge transfer (ICT) process only under the polar conditions of water, indicating its great potential for application as a water sensor.

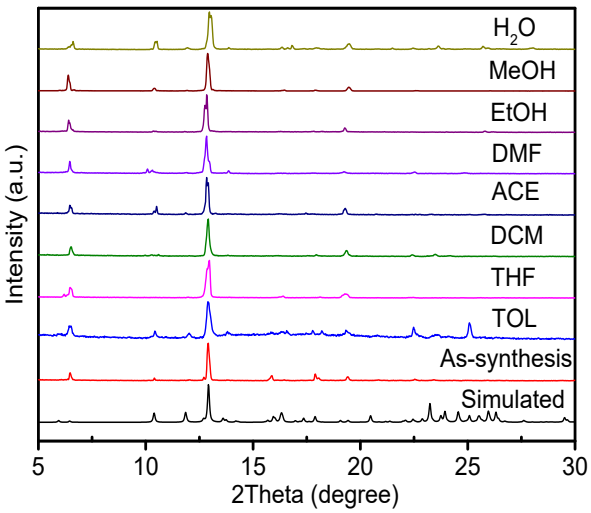

Figure S12. PXRD pattern of **HOF-FJU-167** under the stimulation of different polarity solvents, **HOF-FJU-167**, and **HOF-FJU-167** (simulated).

The powder X-ray diffraction (PXRD) results show that the **HOF-FJU-167** can maintain the crystal structure well under the stimulation of different solvents, and the structure was barely affected during the stimulation process.

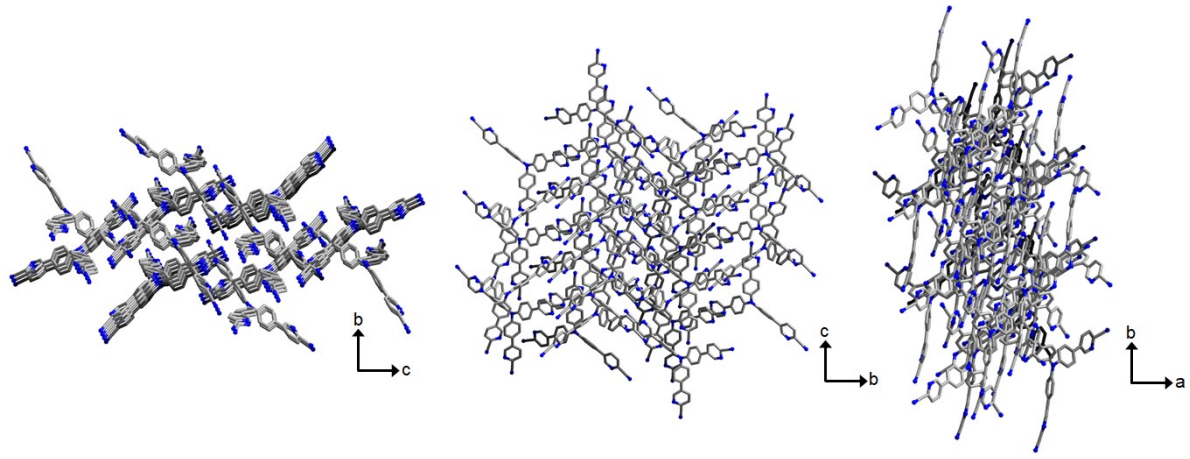

Figure S13. Schematic diagram of the stacking of the **HOF-FJU-167ACE** along different axes.

The channel-free framework (**HOF-FJU-167ACE)** is obtained by the recrystallization of the 5-NBDTP ligand in acetone (ACE). This framework exhibits unique molecular intercalation, flexible intermolecular interactions, and dense packing, which leads to the formation of a non-porous structure. Such a structure hinders the contact between external stimuli and active sites, thereby inhibiting dynamic responsive behavior.

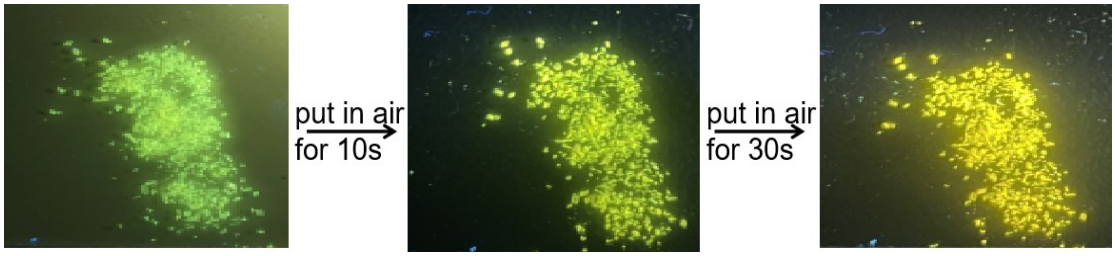

Figure S14. The PL images of **HOF-FJU-167** (initial), in air for 10 s, and 30 s.

To more visually show the fluorescence transformation of **HOF-FJU-167** in air, a large batch of crystals was placed together, and their photoluminescence (PL) images were captured at 10 s and 30 s intervals under ambient conditions.

Figure S15. The PL images of **HOF-FJU-167** under the stimulation of different proton solvents. Scale bar: 50 μm.

The photoluminescence (PL) images of **HOF-FJU-167** stimulated by different proton solvents show that **HOF-FJU-167** has unique selectivity for water.

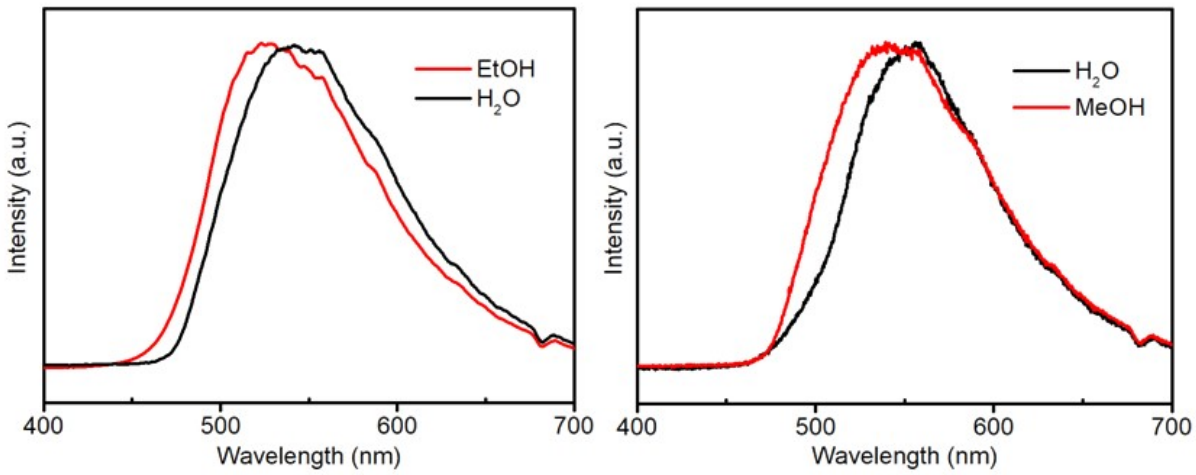

Figure S16. The PL spectra of the **HOF-FJU-167** under the stimulation of water/methanol and water/ethanol.

The photoluminescence (PL) spectra of the **HOF-FJU-167** upon stimulation by water/methanol and water/ethanol were comparatively analyzed. It was found that the emission wavelength of the water-stimulated sample was red-shifted by approximately 30 nm relative to those stimulated by methanol and ethanol, which further confirms the water-selective responsiveness of the **HOF-FJU-167**.

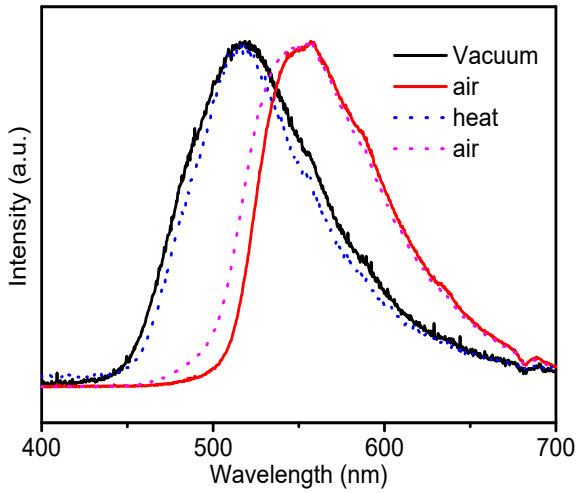

Figure S17. The PL spectra of **HOF-FJU-167** under vacuum/air treatment conditions and heated/air treatment conditions.

The emission peak under vacuum-atmosphere conditions exhibits identical characteristics to that under heating-atmosphere conditions, indicating that both thermal treatment and vacuum treatment can effectively remove water molecules from the framework.

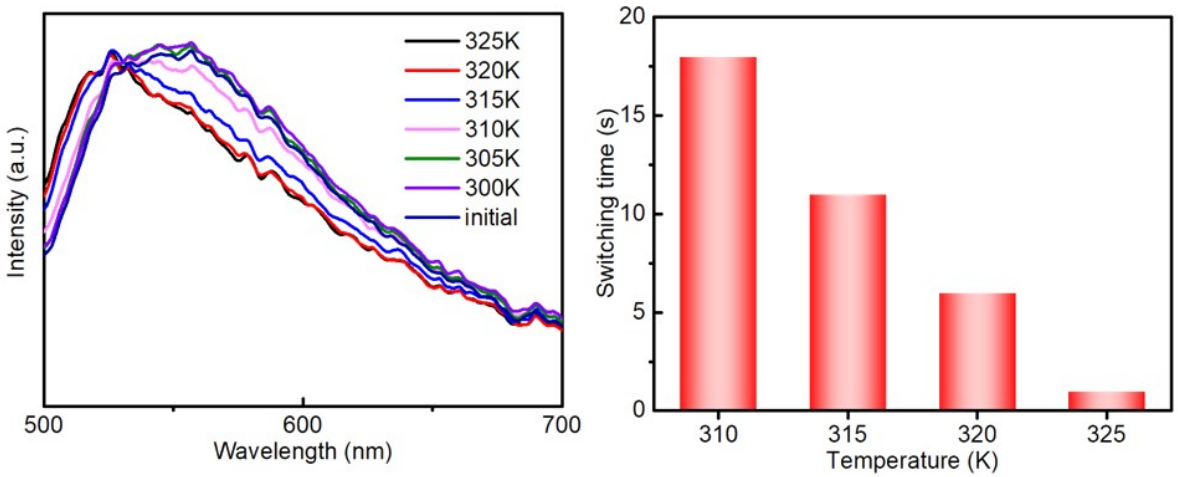

Figure S18. The PL spectra of **HOF-FJU-167H** under different temperature conditions (left) and the schematic diagram of dehydration time under different temperature conditions (right).

As shown in the left figure, *in-situ* photoluminescence (PL) spectra were acquired during the heating process of **HOF-FJU-167H**. A distinct blueshift was observed upon heating to 310 K, signifying the initiation of dehydration, whereas complete dehydration was achieved at 325 K. The right figure provides further insight into the dehydration time frame within the 310-325 K range, with the results showing that dehydration at 325 K is accomplished in merely 1 s. These findings confirm that **HOF-FJU-167H** exhibits rapid dehydration capability under mild thermal conditions.

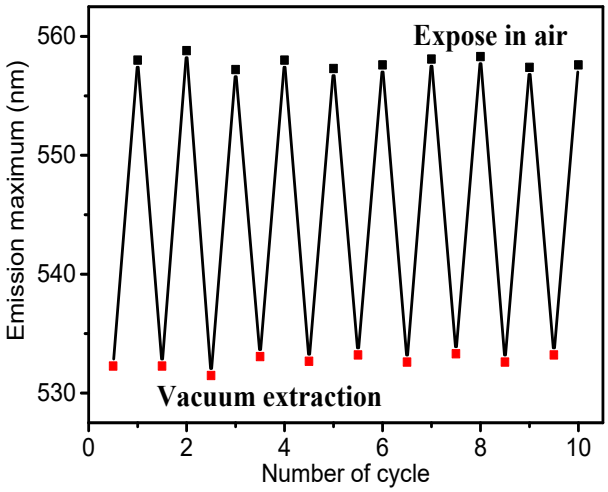

Figure S19. Cyclic diagram of the maximum fluorescence emission under vacuum treatment condition and air treatment condition.

After dozens of vacuum-air treament cycles on the sample, no significant attenuation of the emission peaks was observed, indicating that **HOF-FJU-167** exhibits excellent cyclic stability.

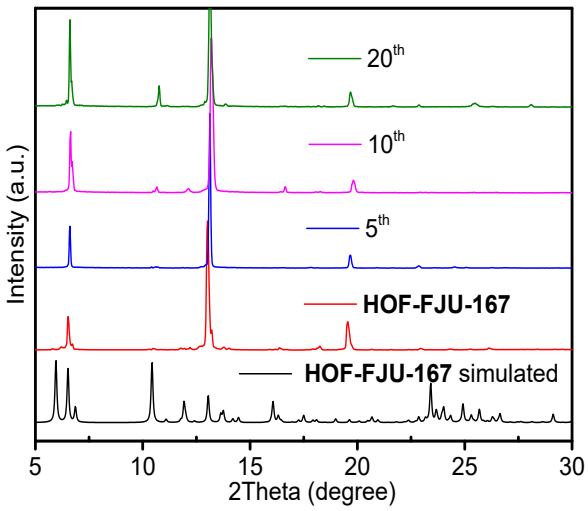

Figure S20. PXRD pattern of **HOF-FJU-167** undergoes several rounds of hydration and dehydration.

The PXRD patterns of several rounds of water absorption and desorption showed the sharp diffraction peaks, which indicated that the **HOF-FJU-167** holds good stability and high crystallinity.

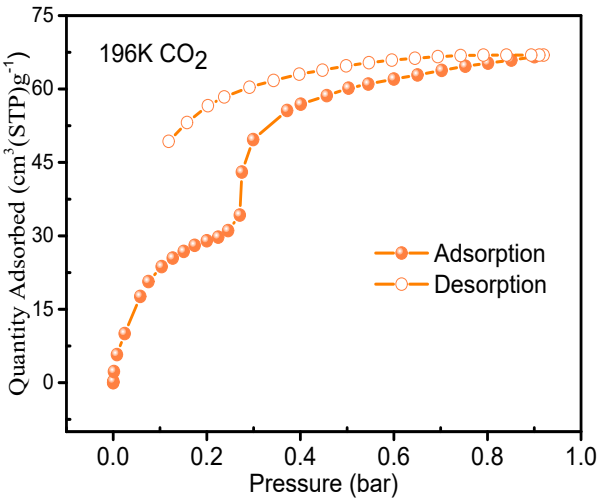

Figure S21. The 196 K CO_2 adsorption isotherm of **HOF-FJU-167**.

The porosity of activated **HOF-FJU-167** was evaluated by CO_2 gas adsorption at 196 K. The CO_2 adsorption isotherm exhibits gently rising adsorption at low pressures (<0.3 bar), with a significant increase in adsorption at pressures exceeding 0.3 bar, indicative of the dynamic framework nature of **HOF-FJU-167**.

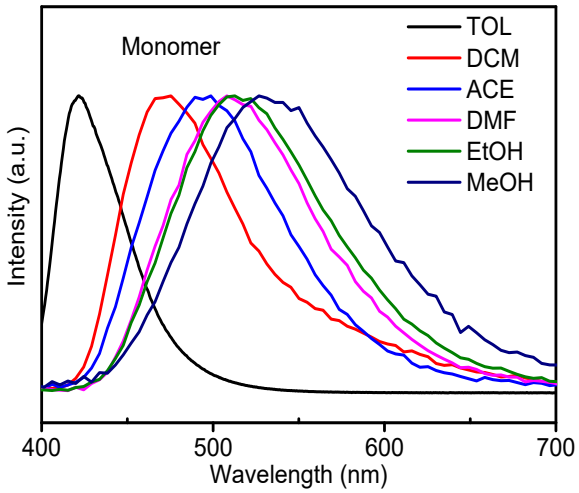

Figure S22. The PL spectra of the monomer (4-NBDTP) dissolved in solvents of different polarities.

The photoluminescence (PL) spectra of the monomer dissolved in solvents of different polarities show an emission redshift as the polarity increases, which demonstrates that the building unit possesses an intrinsic intramolecular charge transfer (ICT) characteristic.

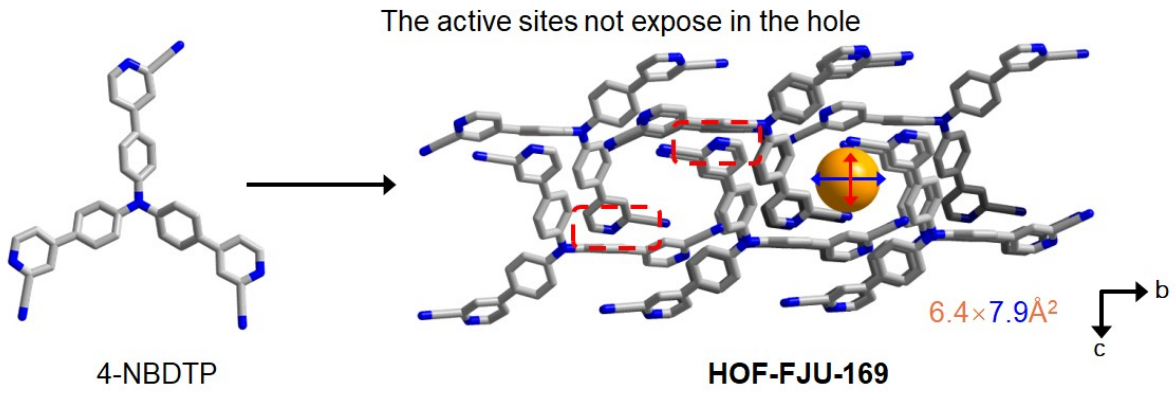

Figure S23. Schematic Diagrams of 4-NBDTP and **HOF-FJU-169**.

HOF-FJU-169 features a channel with a size of 6.4 × 7.9 Å², providing an ideal channel for guest molecules to enter and exit freely. However, its pyridine-based active sites are not located within the channel cavity, preventing the framework from responding to external stimuli and thus precluding the realization of the dynamic single-molecule-like emission.

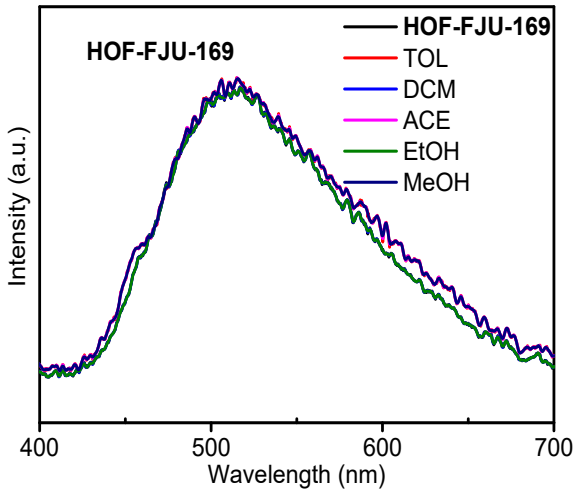

Figure S24. The PL spectra of **HOF-FJU-169** under the stimulation of different polar solvents.

The **HOF-FJU-169** constructed by the building unit (4-NBDTP) was stimulated by solvents of different polarities, which shows the same emission wavelength, exhibiting the phenomenon that **HOF-FJU-169** is unable to retain the ICT characteristic.

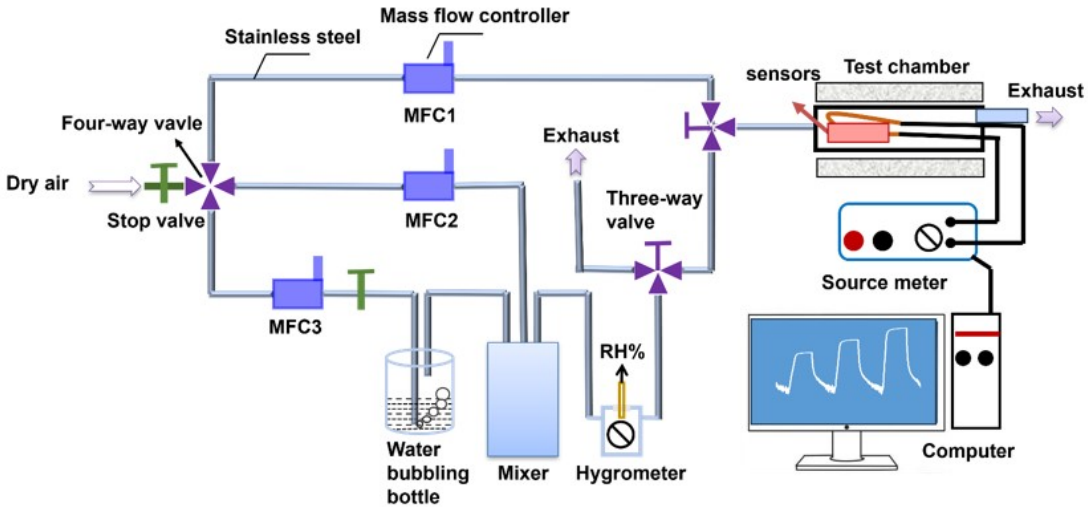

Figure S25. Schematic diagram of the homemade setup used to measure the humidity sensor performance at 98 % RH.

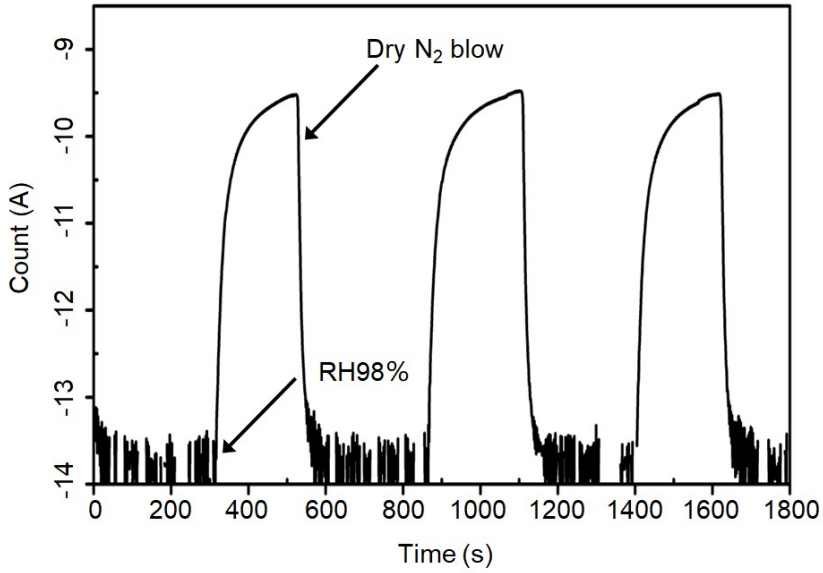

Figure S26. Real-time dynamic response-recovery curves of **HOF-FJU-167** when alternating dry N_2 and 98 % RH N_2.

The current peak did not drop significantly after three cycles, demonstrating that the voltage load and water vapor fumigation did not damage the devices.

Table S1. Crystal data and structure refinement for the **HOF-FJU-167** (CCDC No. 2502738), **HOF-FJU-167H** (CCDC No. 2502741), **HOF-FJU-167ACE** (CCDC No. 2502742), and **HOF-FJU-169** (CCDC No. 2502743).

Identification code	HOF-FJU-167	HOF-FJU-167H	HOF-FJU-167ACE	HOF-FJU-169
Empirical formula	C36H21N7	C36H25N7O2.91	C36H21N7	C36H21N7
Formula weight	551.6	602.19	551.6	551.6
Temperature/K	290.35(10)	223(10)	292.23	150.00(10)
Crystal system	triclinic	triclinic	triclinic	triclinic
Space group	P-1	P-1	P-1	P-1
a/Å	7.6631 (6)	7.4610 (5)	10.1070 (6)	10.1151 (3)
b/Å	15.2276 (10)	15.0917 (3)	24.7994 (14)	11.3484 (3)
c/Å	16.2344 (12)	16.0554 (10)	11.7457(6)	14.2158 (4)
α/°	113.093 (7)	113.088 (2)	90	111.469 (3)
β/°	90.821 (6)	91.881 (5)	106.324(6)	93.950 (2)
γ/°	100.965 (6)	101.197(5)	90	99.324 (2)
Volume/ Å^3	1702.5 (2)	1619.43 (5)	2825.3(3)	1483.88 (8)
Z	7	2	12	2
pcalc g/cm^3	1.176	1.235	1.214	1.235
μ/mm^{-1}	0.605	0.661	0.625	0.601
F (000)	639.1	627.0	1092.0	572.0
Crystal size/mm^3	0.15×0.05×0.02	0.15×0.05×0.02	0.15×0.05×0.02	0.15×0.05×0.02
Radiation	Cu Kα (λ=1.54184)	Cu Kα (λ=1.54184)	Cu Kα (λ=1.54184)	Cu Kα (λ=1.54184)
2θ range for data	5.94 to 145.58	6.028 to 152.53	7.13 to 145.516	6.748 to 127.072
Index ranges	-8≤ h ≤9,-17≤ k ≤18,-19 ≤l≤ 19	-7≤ h ≤9,-18≤ k ≤18,-19 ≤l≤ 19	-11≤ h ≤12,-30≤ k ≤27,-12 ≤l≤ 14	-11≤ h ≤11,-13≤ k ≤11,-16 ≤l≤ 16
Reflections collected	12760	16959	12890	13403
Independent reflections	6559[R_{int}=0.0483,R_{sigma}=0.0429]	6369[R_{int}=0.0478,R_{sigma}=0.0386]	5276[R_{int}=0.0620,R_{sigma}=0.0728]	4719[R_{int}=0.0368,R_{sigma}=0.0406]
Data/restraints/parameters	6559/0/389	6369/12/460	5276/12/398	4719/0/388
Goodness-of-fit on F^2	1.004	1.064	1.056	1.183
Final R indexes [I >=2σ (I)]	R1=0.0635,wR2=0.1695	R1=0.0923,wR2=0.2808	R1=0.0841,wR2=0.2157	R1=0.0605,wR2=0.1937
Final R indexes [all data]	R1=0.0971,wR2=0.2064	R1=0.1049,wR2=0.2926	R1=0.1382,wR2=0.2741	R1=0.0808,wR2=0.2011
Largest diff. peak/hole/e Å^{-3}	0.27/-0.28	1.01/-0.33	0.36/-0.24	0.32/-0.31

Table S2. Emission maxima of **HOF-FJU-167** under the stimulation of different solvent atmospheres.

Solvent atmosphere	λ_{em} (nm)
HOF-FJU-167	514
TOL	499
CB	500
THF	516
DCM	523
EtOH	525
IPA	517
NPA	516
MeOH	532
H_2O	556

Table S3. Emission maxima of **HOF-FJU-167** under different humidity conditions.

Relative humidity	λ_{em} (nm)
0 %	514
12 %	521
21 %	529
55 %	531
84 %	542
100 %	556